IEICE TRANS. ELECTRON., VOL.E84–C, NO.12 DECEMBER 2001

PAPER Special Issue on New Technologies in Signal Processing for Electromagnetic-wave Sensing and Imaging

Polarimetric Characteristics of Forest at Coherent Decomposition in Polarimetric SAR Interferometry

Koichi SATO†, *Student Member*, Hiroyoshi YAMADA†, *and* Yoshio YAMAGUCHI†a), *Regular Members*

SUMMARY In this paper, we examine the polarimetric characteristics and the potential of the coherent decomposition in polarimetric synthetic aperture radar (SAR) interferometry. Coherent scattering decomposition based on the coherence optimization can separate effective phase center of different scattering mechanisms and can be used to generate canopy digital elevation model (DEM). This decomposition is applied to a simplified stochastic scattering model such as forest canopy. However, since the polarimetric characteristics are not well understood when the decomposition is carried out, we investigate its characteristics and potential using polarimetric entropy-alpha and three-component scattering matrix decomposition. The results show that the first and third components correspond to the lower and upper layer, respectively, in ideal case. In this investigation, SIR-C/X-SAR data of the Tien Shan flight-pass are used.

key words: *radar polarimetry, SAR interferometry, polarimetric interferometry, coherent decomposition*

1. Introduction

SAR interferometry [1]–[5] is a technique to measure accurate terrain topography using phase difference from slightly different orbits, and is sensitive primarily to spatial distribution. On the other hand, radar polarimetry [6]–[10] is a technique to measure polarization properties of the scattered waves corresponding to targets, and is sensitive primarily to the shape and orientation of the scatterers [13]. These techniques can be applied to various fields such as geology, geophysics and ecosystem dynamics.

Cloude and Papathanassiou reported the first application of polarimetic interferometry that combines both radar polarimetry and SAR interferometry [11]. Their coherence optimization [11] can enhance the quality of SAR interferogram by selecting optimum polarizaion, which leads to coherent decomposition. Furthermore, discriminated scattering centers by this method relate to the effective phase centers of scattering mechanism. The optimization technique is employed in the inversion algorithm for the forest height estimation [12], [14]. However, there still remains an interesting problem how the optimization and decomposition work for polarimetric characteristics of each target.

The objective of this paper is to examine the polarimetric characteristics of the coherency matrix before and after the decomposition. It is important to understand the difference of the polarimetric characteristics, because it could be used for locating the phase center in the three-layer model. In order to examine the polarimetric effect in the decomposition scheme, we transformed the coherency matrix using decomposed eigenvector (scattering mechanism). Then we analyzed the polarimetric change of the matrix by the decomposition using two techniques: polarimetric entropy-alpha [9], [10], and three-component scattering matrix decomposition [6], [7]. As a result, it turned out that the first and third components correspond to the lower and upper layer, respectively, in ideal case.

The paper is organized as follows. Section 2 describes the coherence optimization, the decomposition algorithm, and a new decomposed coherency matrix in polarimetric interferometry. Section 3 summarizes polarimetric analysis methods. Section 4 shows the results obtained by these methods, and discuss the polarimetric characteristic change and the potential. Finally, in Sect. 5, we present the conclusions. In these analysis, SIR-C/X-SAR L-Band single-look complex (SLC) data of the Tien Shan flight-pass are used.

2. Polarimetric Interferometry

2.1 Interferometric Phase and Coherence

In fully polarimetric observations, the scattering matrix $[S]$ is measured using two linearly polarized antennas.

$$[S] = \begin{bmatrix} S_{HH} & S_{HV} \\ S_{VH} & S_{VV} \end{bmatrix} \tag{1}$$

To generalize the expressions for the interferometric phase and the coherence, the trace of the product (scattering matrix $[S]$ and Pauli matrix Ψ_p) is employed, then the coherent scattering vector can be expressed by $\boldsymbol{k} = 1/2\ Trace([S]\Psi_p)$. The reciprocity theorem constrains the scattering matrix to be symmetric, i.e., $S_{HV} = S_{VH}$, and coherent vector $\boldsymbol{k}$ can be simplified as [9]

$$\boldsymbol{k} = \frac{1}{\sqrt{2}} \begin{bmatrix} S_{HH} + S_{VV} \\ S_{HH} - S_{VV} \\ 2S_{HV} \end{bmatrix}. \tag{2}$$

Manuscript received March 27, 2001.

†The authors are with Niigata University, Niigata-shi, 950-2181 Japan.
a) E-mail: yamaguch@ie.niigata-u.ac.jp

Polarimetric properties for each image can be represented in the form of Hermitian coherency matrices, $[T_{11}]$ and $[T_{22}]$, while polarimetric and interferometric information can be described as a non-Hermitian coherency matrix $[\Omega_{12}]$.

$$[T_{11}] = \left\langle \boldsymbol{k}_1 \boldsymbol{k}_1^{*T} \right\rangle$$
$$[T_{22}] = \left\langle \boldsymbol{k}_2 \boldsymbol{k}_2^{*T} \right\rangle$$
$$[\Omega_{12}] = \left\langle \boldsymbol{k}_1 \boldsymbol{k}_2^{*T} \right\rangle \tag{3}$$

where * and ^{T} indicate complex conjugation and transpose operation, respectively. Introducing two normalized complex vectors, $\boldsymbol{w}_1$ and $\boldsymbol{w}_2$, that can be interpreted as generalized scattering mechanisms, a semidefinite coherency matrix $[J]$ is give by [11]

$$[J] = \begin{bmatrix} \boldsymbol{w}_1^{*T}[T_{11}]\boldsymbol{w}_1 & \boldsymbol{w}_1^{*T}[\Omega_{12}]\boldsymbol{w}_2 \\ \boldsymbol{w}_2^{*T}[\Omega_{12}]^{*T}\boldsymbol{w}_1 & \boldsymbol{w}_2^{*T}[T_{22}]\boldsymbol{w}_2 \end{bmatrix}. \tag{4}$$

From Eq. (4) the generalized expression for interferometric phase Φ and coherence γ are given by

$$\Phi = Arg\left(\boldsymbol{w}_1^{*T}\left[\Omega_{12}\right]\boldsymbol{w}_2\right) \tag{5}$$

$$\gamma = \frac{\left|\left\langle \boldsymbol{w}_1^{*T}\left[\Omega_{12}\right]\boldsymbol{w}_2\right\rangle\right|}{\sqrt{\left\langle \boldsymbol{w}_1^{*T}\left[T_{11}\right]\boldsymbol{w}_1\right\rangle\left\langle \boldsymbol{w}_2^{*T}\left[T_{22}\right]\boldsymbol{w}_2\right\rangle}}. \tag{6}$$

2.2 Coherence Optimization

The coherence optimization is to select these scattering mechanisms, $\boldsymbol{w}_1$ and $\boldsymbol{w}_2$, that maximize the interferometric coherence defined in Eq. (6). This problem is equivalent to solving complex eigenvalue problems of the following equations for the vectors $\boldsymbol{w}_1$ and $\boldsymbol{w}_2$.

$$[T_{11}]^{-1}[\Omega_{12}][T_{22}]^{-1}[\Omega_{12}]^{*T}\boldsymbol{w}_1 = \lambda \boldsymbol{w}_1 \tag{7}$$

$$[T_{22}]^{-1}[\Omega_{12}]^{*T}[T_{11}]^{-1}[\Omega_{12}]\boldsymbol{w}_2 = \lambda \boldsymbol{w}_2 \tag{8}$$

Since the eigenvalues are real, the optimized coherence is given by the maximum eigenvalue.

$$\gamma_{max} = \sqrt{\lambda_{max}} \tag{9}$$

2.3 Coherent Decomposition

Equations (7) and (8) can be rewritten as a sum of three component vectors $(\boldsymbol{w}_{1j}, \boldsymbol{w}_{2j}, (j = 1, 2, 3))$ weighted by their appropriate eigenvalues, and given by [11]

$$[T_{11}]^{-1}[\Omega_{12}][T_{22}]^{-1}[\Omega_{12}]^{*T} = \lambda_1(\boldsymbol{w}_{11}\boldsymbol{w}_{11}^{*T}) + \lambda_2(\boldsymbol{w}_{12}\boldsymbol{w}_{12}^{*T}) + \lambda_3(\boldsymbol{w}_{13}\boldsymbol{w}_{13}^{*T}) \tag{10}$$

$$[T_{22}]^{-1}[\Omega_{12}]^{*T}[T_{11}]^{-1}[\Omega_{12}] = \lambda_1(\boldsymbol{w}_{21}\boldsymbol{w}_{21}^{*T}) + \lambda_2(\boldsymbol{w}_{22}\boldsymbol{w}_{22}^{*T}) + \lambda_3(\boldsymbol{w}_{23}\boldsymbol{w}_{23}^{*T}). \tag{11}$$

Six eigenvectors, $\boldsymbol{w}_{1j}$ for image 1 and $\boldsymbol{w}_{2j}$ for image 2, can be derived by the coherence decomposition (in Eqs. (10) and (11)). As described in [11], the vectors, $\boldsymbol{w}_{1j}$ and $\boldsymbol{w}_{2j}$, represent scattering mechanisms interpreted as statistically independent.

2.4 Decomposed Coherency Matrix

Outline of the coherence optimization and the coherent decomposition by polarimetric information is described in the previous subsection.

Here we consider derivation of the polarimetric characteristics from the optimized or decomposed matrices. In order to derive the polarimetric characteristics, we define a new decomposed coherency matrix $[C_{ii}]$ using $\boldsymbol{w}_{ij}$.

Let us define a diagonal matrix $[W_i]$ whose elements are composed of the scattering mechanisms $\boldsymbol{w}_i$ $(i = 1, 2)$ in the previous Sect. 2.3. Then the original coherency matrix $[T_{ii}]$ is filtered by the diagonal matrix $[W_i]$ as shown in Eq. (14).

$$\boldsymbol{w}_i = \begin{bmatrix} w_{i1} & w_{i2} & w_{i3} \end{bmatrix}^T \tag{12}$$

$$[W_i] = \begin{bmatrix} w_{i1} & 0 & 0 \\ 0 & w_{i2} & 0 \\ 0 & 0 & w_{i3} \end{bmatrix} \tag{13}$$

$$[C_{ii}] = [W_i]^{*T}[T_{ii}][W_i] \tag{14}$$

Now it is possible to apply Eq. (14) directly to the polarimetric decomposition, because the filtered matrix $[C_{ii}]$ is also Hermitian coherency matrix whose elements represent scattering mechanisms optimized or decomposed by the previous techniques.

3. Polarimetric Analysis Methods

3.1 Polarimetric Entropy-Alpha [9]

The coherency matrix $[T]$ has the advantage of relating to physical scattering mechanisms. The matrix $[T]$ can be decomposed into the following equation.

$$[T] = \nu_1(\boldsymbol{e}_1\boldsymbol{e}_1^{*T}) + \nu_2(\boldsymbol{e}_2\boldsymbol{e}_2^{*T}) + \nu_3(\boldsymbol{e}_3\boldsymbol{e}_3^{*T}) \tag{15}$$

where ν_i are the eigenvalues of $[T]$ and $\boldsymbol{e}_i$ are the corresponding eigenvectors $(i = 1, 2, 3)$, which can be written as

$$\boldsymbol{e}_i = \begin{bmatrix} \cos\alpha_i \\ \sin\alpha_i \cos\beta_i e^{i\delta_i} \\ \sin\alpha_i \sin\beta_i e^{i\gamma_i} \end{bmatrix}. \tag{16}$$

The α angle is defined with range $0° \leq \alpha \leq 90°$ and can be used to represent physical scattering mechanism. $\alpha = 0°$ can be interpreted as a surface scattering. As

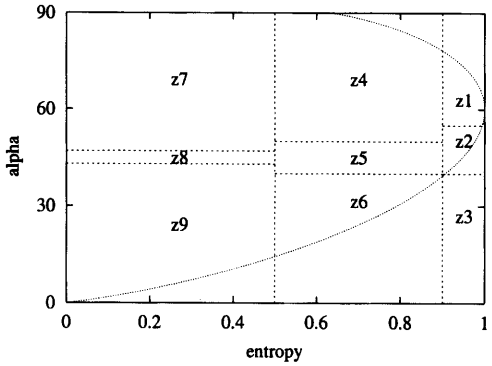

Fig. 1 H-α plane.

α increases, the surface scattering becomes anisotropic. In $\alpha = 45°$, we have dipole scatterers in which one of the copolarized scattering coefficients goes to zero. In case of $\alpha > 45°$, it can be considered as the scattering by anisotropic dihedrals. In the limit $\alpha = 90°$, we obtain isotropic double (or even) bounce scattering mechanisms.

The entropy H (ranging from 0 to 1) which represents randomness of the scattering medium is defined by

$$H = -\sum_{i=1}^{3} P_i \log_3 P_i \quad \text{where} \quad P_i = \frac{\nu_i}{\sum_{j=1}^{3} \nu_j} \tag{17}$$

When the entropy H is low, the medium is expected to be weakly depolarized. Whereas when the entropy H is high, the medium is depolarized. Similarly, averaged alpha $\bar{\alpha}$ is defined as follows,

$$\bar{\alpha} = \sum_{i=1}^{3} P_i \alpha_i. \tag{18}$$

These values, H and $\bar{\alpha}$, are often plotted in a 2D-plane (Fig. 1) and are utilized for analysis of scattering nature of terrain.

3.2 Three-Component Scattering Matrix Decomposition

In symmetric scattering matrix, it is possible to decompose the scattering matrix into polarimetric three basic-components, i.e., sphere, diplane, and helix component matrix [6]. The relation between the original scattering matrix and the component matrices can be expressed by [6]–[8]

$$\begin{aligned}[S(HV)] = {} & K_s e^{j\varphi_s} \begin{bmatrix} 1 & 0 \\ 0 & 1 \end{bmatrix} \\ & + K_d e^{j(\varphi_s+\varphi_r)} \begin{bmatrix} \cos 2\theta_d & \sin 2\theta_d \\ \sin 2\theta_d & -\cos 2\theta_d \end{bmatrix} \\ & + K_h e^{j(\varphi_s+\varphi_r)} \frac{1}{2} \begin{bmatrix} 1 & \pm j \\ \pm j & -1 \end{bmatrix} \end{aligned} \tag{19}$$

Table 1 Relation between magnitude ratio and elementary targets.

	K_s	K_d	K_h
sphere, plate	1	0	0
diplane	0	1	0
dipole	0.5	0.5	0
right or left helix	0	0	1

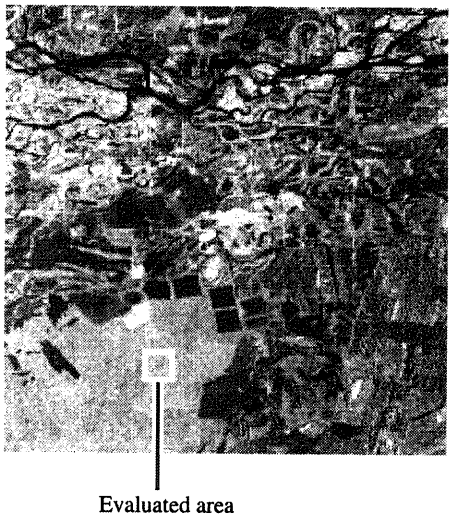

Fig. 2 Total power image. The rectangular region shows the selected area for evaluation as forest.

where the factors K_s, K_d and K_h represent the magnitude contribution of sphere, diplane and helix component, respectively. Ratio of each contribution can be evaluated by

$$\frac{K_i}{K_s + K_d + K_h} \quad (i = s, d, h). \tag{20}$$

This factors can be utilized to classify the target into four elementary targets listed in Table 1. The decomposition is easily carried out in the LR basis [7], and can be directly applied to the new coherency matrix $[C_{ii}]$ also.

4. The Polarimetric Characteristics

The objective of this section is to discuss the polarimetric characteristics of the decomposed coherency matrices. The polarimetric entropy-alpha and the three-component scattering matrix decomposition techniques are used to analyze polarimetric characteristics of scatterers within canopy. In this experiment, SIR-C/X-SAR L-Band SLC data pairs of Tien Shan flight-pass on October 8 and 9, 1994 are used (Fig. 2). The forest area is located at lower left of the image, and the smooth area is extended from center to upper region of the image. Furthermore in the upper part around the Selenga River, there are shrub-land areas. Radar polarimetry is sensitive primarily to the shape and orientation of the forest scatterers, whereas interferometry

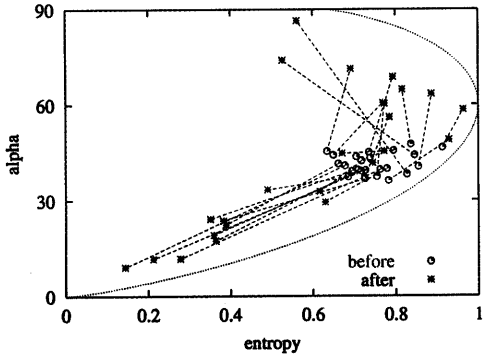

(a) Original and 1st components

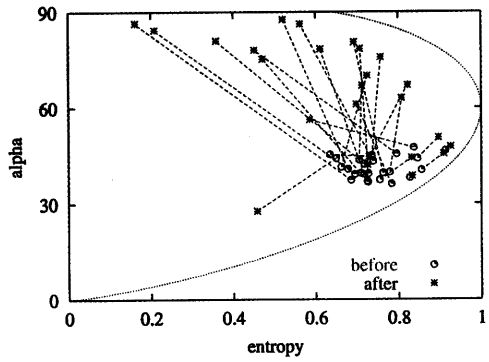

(b) Original and 2nd components

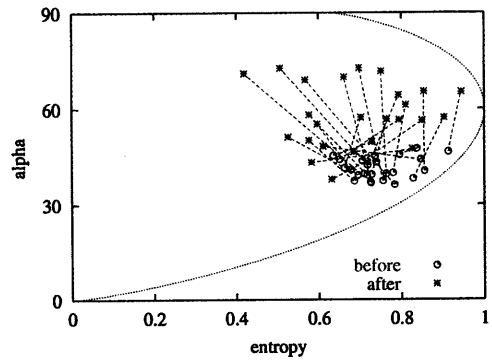

(c) Original and 3rd components

Fig. 3 Changes of H, $\bar{\alpha}$ before and after the coherent decomposition of the forest.

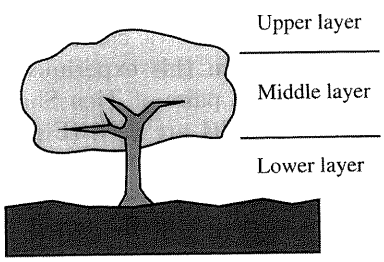

Fig. 4 Three-layer model.

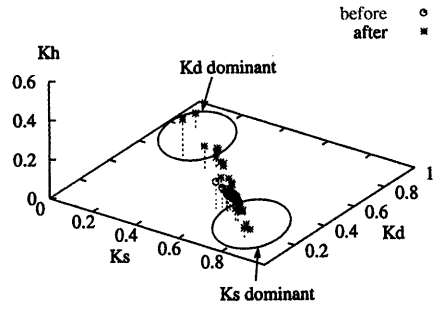

(a) Original and 1st components

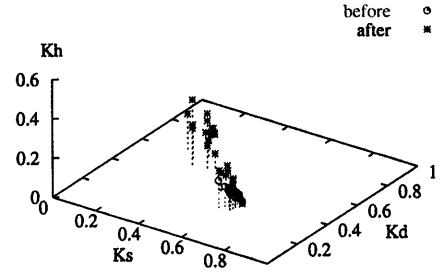

(b) Original and 2nd components

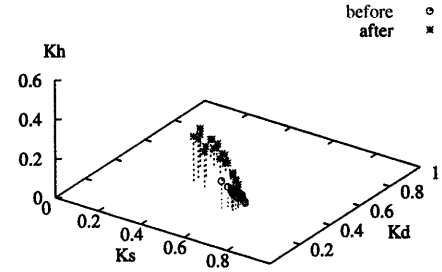

(c) Original and 3rd components

Fig. 5 Changes of three-component, before and after the coherent decomposition of the forest.

is sensitive primarily to the spatial distribution of the forest [13]. Therefore polarimetric interferometry can analyze scattering characteristics of the forest by utilizing each technique.

4.1 Entropy H-Alpha Plane

Nine zones defined by Cloude and Pottier in H-α plane [10] are useful for interpreting observed forest structures in this experiment. If entropy is low, e.g., $H < 0.5$ (zone 7–zone 9), these zones are considered as the area with thin branches and trunks, or sparse tree. On the other hand, the zones of $H > 0.5$ (zone 1–zone 6) cor-

respond to the area of dense forest. Therefore, each zone can be interpreted as follows in the entropy-alpha analysis.

Zone 9: This zone corresponds to surface scatterer, or thin spatially-distributed scatterer and the smooth ground. **Zone 8**: This zone has scattered waves from isolated dipoles (e.g., branches and small trunks). Their vertical distribution can be also assumed to be thin. **Zone 7**: This zone has dominant double bounce scattering waves of branch-trunk, ground-crown, and grand-trunk interaction. These components can be observed at L- and C-Band radars. **Zone 6**: This zone includes smooth surface scatterer propagated through dense canopy. **Zone 5**: This zone has dominant dipole scatterers. **Zone 4**: This zone is almost similar to zone 7, however, scattered waves are highly affected by propagation through the canopy. **Zone 3**: No scattered waves can be classified in this zone because of the scattering nature. **Zone 2**: The waves classified in this zone occur by scatterers from dense canopy and its dipole particles. However the waves could be often affected by random noise. **Zone 1**: This zone has double bounce components that are generated by propagation through dense canopy similar to zone 2.

Figures 3(a)–(c) show change of entropy-alpha before and after the coherent decomposition. Using the zones mentioned above, we can interpret the results (Fig. 3) of entropy-alpha analysis in the forest. The first (dominant) components are mainly plotted in zones 9, 6, and 4. Most of the second components are plotted in zones 7 and 4. The third components are plotted in zones 7, 5, and 4. In the original (before the decomposition) components can be considered to be mixed scatterer of spheres (backscatter from the ground), multiple bounces (e.g., grand-trunk or grand-canopy interaction) and helices. After the decomposition processing, the mixed components can be decomposed into local components corresponding to the scattering mechanism of local scattering center. These decomposed results explain local scattering mechanisms in the forest easily.

4.2 Interpretation of Decomposed Components

Let us consider the relation between the decomposed local scattering centers and the scattering mechanisms derived from the three-layer model (Fig. 4). The dominant scattering in the lower layer is caused by the surface reflection. The middle layer is the region inside the canopy where multiple scattering (random volume scattering) occurs. The upper layer is the canopy region of direct scattering. The first (dominant) components are mainly located at the lower layer. Since the microwave at L-Band reaches the ground through the canopy, the optimization algorithm tends to maximize the ground-to-volume amplitude ratio [12]. Therefore when scattering waves in zone 4 are generated by ground-trunk interaction and their polarization states are orthogonal to those of the volume scattering, the scattering centers of the first components locate on the ground (in the lower layer). Since zones 7 and 4 represent double or even bounce scatterer, (e.g., trunk-branch or branch-branch interaction,) the scattering centers of the second components locate between the upper and lower layer. The third components are more similar to dipole components than the second components. Therefore in ideal case when the polarization states of the waves from canopy and the ground are orthogonal, the third components correspond to the upper layer.

4.3 Interpretation Using Three-Component Scattering Matrix Decomposition

Next we examine polarimetric characteristics estimated by the three-component scattering matrix decomposition. Figures 5(a)–(c) show the decomposed results. Before the coherent decomposition, each pixel has dipole-like property ($K_s = K_d, K_h = 0$). After the coherent decomposition, K_h ratio increases in the third components (Fig. 5(c)). In addition, K_s and K_d appear with almost the same ratio. This characteristic shows the typical mixture of dipole scattering in the forest canopy.

On the other hand, some featuring points appear in the first components after the coherent decomposition in Fig. 5(a), where K_s ratio is dominant or K_d ratio is dominant. This distribution is different from that of the third components (canopy scattering). Since K_s and K_d represent single and double bounce reflection, respectively, this effect may be caused by ground surface, and tree trunk-ground reflection. Although other decomposed points exist in Fig. 5(a), they may be caused by polarization change through the canopy. Therefore the first components correspond to scatterers from lower layer.

5. Conclusions

In this paper we have examined the polarimetric characteristics and the potential at the coherent decomposition in polarimetric SAR interferometry. Polarimetric entropy-alpha and three-component scattering matrix decomposition were used to examine the characteristics of local scattering from the forest region. The results can be interpreted using three-layer model of the canopy. It seems that the first and the third components have the scattering properties in the upper (the canopy) layer and in the lower (the ground) layer, respectively. When polarization states of the scatterers in the upper and the lower layer are not orthogonal, the decomposition technique cannot resolve the scatterers properly, then physical interpretation also becomes difficult. To estimate polarization state of local scatterer more precisely, some modification will be required. It is an important problem to be solved for improving the

advantages of polarimetric SAR interferometry.

Acknowledgement

This work in part was supported by Grant-in-Aid for Scientific Research, Ministry of Education, Japan.

References

[1] D. Massonnet and T. Rabaute, "Radar interferometry: Limit and potential," IEEE Trans. Geosi. Remote Sensing, vol.31, no.2, pp.455–464, March 1993.
[2] Q. Lin, J.F. Veseccky, and H.A. Zebker, "New approaches in interferometic SAR data processing," IEEE Trans. Geosi. Remote Sensing, vol.30, no.3, pp.560–567, May 1992.
[3] R. Lanari, G. Fornaro, D. Riccio, and M. Migliaccio, "Generation of digital elevation models by using SAR-C/X-SAR multifrequency two-pass interferometry: The etna case study," IEEE Trans. Geosi. Remote Sensing, vol.34, no.5, pp.1097–1114, Sept. 1996.
[4] H.A. Zebker, T.G. Farr, R.P. Salazar, and T.H. Dixon, "Mapping the world's topography using radar interferometry: The TOPSAT mission," Proc. IEEE, vol.82, no.12, pp.1774–1786, Dec. 1994.
[5] R.H. Treuhaft, S.N. Madsen, M. Moghaddam, and J.J. van Zyl, "Vegetation characteristics and surface topography from interferometric radar," Radio Sci., vol.31, pp.1449–1485, Nov./Dec. 1996.
[6] E. Krogager, Aspect of polarimetric radar imaging, Ph.D. dissertation, Danish Defence Research Establishment, 1993.
[7] E. Krogager and Z.H. Czyz, "Properties of the sphere, diplane, helix decomposition," Proc. 3rd International Workshop on Radar Polarimetry, pp.106–115, March 1995.
[8] Y. Yamaguchi, Fundamentals of polarimetric radar and its applications, Realize Inc., 1998.
[9] S.R. Cloude and E. Pottier, "A review of target decomposition theorems in radar polarimetry," IEEE Trans. Geosi. Remote Sensing, vol.34, no.2, pp.498–518, March 1996.
[10] S.R. Cloude and E. Pottier, "An entropy based classification scheme for land applications of polarimetric SAR," IEEE Trans. Geosi. Remote Sensing, vol.35, no.1, pp.68–78, Jan. 1997.
[11] S.R. Cloude and K.P. Papathanassiou, "Polarimetric SAR interferometry," IEEE Trans. Geosi. Remote Sensing, vol.36, no.5, pp.1551–1565, Sept. 1998.
[12] K.P. Papathanassiou and S.R. Cloude, "Vegetation and ground parameter estimation using polarimetric interferometry part 1/2," Proc. ESA CEOS SAR Workshop, Toulouse, France, Oct. 1999.
[13] R.N. Treuhaft and P.R. Siqueira, "Vertical structure of vegetated land surfaces from interferometric and polarimetric radar," Radio Sci., vol.35, pp.141–177, Jan./Feb. 1998.
[14] R.N. Treuhaft and S.R. Cloude, "The structure of oriented vegetation from polarimetric interferometry," IEEE Trans. Geosi. Remote Sensing, vol.37, no.5, pp.2620–2624, Sept. 1999.
[15] K.P. Papahtanassiou, A. Reigber, R. Sheiber, A. Moreira, and S.R. Cloude, "Airborne polarimetric SAR interferometry," Proc. IGARSS 1998, Singapore, Aug. 1997.

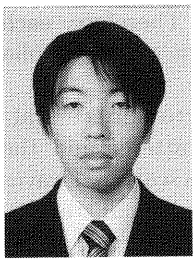

Koichi Sato was born in Niigata Prefecture, Japan, on February 13, 1978. He received the B.E. degree in information engineering from Niigata University, Niigata, Japan, in 2000. He is now a graduate student pursuing the M.E. degree at Niigata University, where he is engaged in SAR interferometry and radar polarimetry.

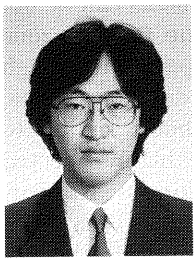

Hiroyoshi Yamada received the B.E, M.E. and Dr.Eng. degrees from Hokkaido University, Sapporo, Japan, in 1988, 1990 and 1993, respectively, all in electronic engineering. In 1993, he joined the Faculty of Engineering, Niigata University, where he is an associate professor. From 2000 to 2001, he was a Visiting Scientist at Jet Propulsion Laboratory, California Institute of Technology, Pasadena. His current interests involve in the field of array signal processing, radar polarimetry and interferometry, microwave remote sensing and imaging. Dr. Yamada is a member of IEEE.

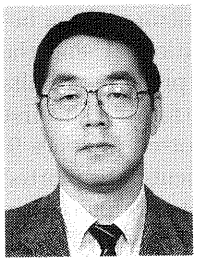

Yoshio Yamaguchi received the B.E. degree in electronics engineering from Niigata University in 1976, and the M.E. and Dr.Eng. degrees from Tokyo Institute Technology in 1978 and 1983, respectively. In 1978, he joined the Faculty of Engineering, Niigata University, where he is a professor. From 1988 to 1989, he was a Research Associate at the University of Illinois, Chicago. His interests are in the field of propagation characteristics of electromagnetic waves in lossy medium, radar polarimetry, microwave remote sensing and imaging. Dr. Yamaguchi is a senior member of IEEE, and a member of the Japan Society for Snow Engineering.